CHEMISTRY OF MATERIALS

pubs.acs.org/cm

Article

Phase Behavior and Electrical Transport in DBTTF:HATCN Donor−Acceptor Mixtures

Andreas Opitz,* Hongwon Kim, Dmitry Lapkin,* Gianfranco Melis, Ainur Abukaev, Marie Siegert, Lennart Frohloff, Lisa Schraut-May, Oleg Konovalov, Alexander Hinderhofer, Frank Schreiber, Jens Pflaum, and Wolfgang Brütting*

Cite This: *Chem. Mater.* 2026, 38, 4726−4737

Read Online

ACCESS | Metrics & More | Article Recommendations | Supporting Information

ABSTRACT: The formation of donor−acceptor complexes (DACs) between the electron donor Dibenzotetrathiafulvalene (DBTTF) and the acceptor Hexaazatriphenylenehexacarbonitrile (HATCN) results in a separated phase with a distinctly different crystal structure as well as optical absorption bands below the energy gaps of the two pristine materials. X-ray scattering and atomic force microscopy provide detailed insights into the film structure and morphology by systematic variation of the mixing ratio from pristine DBTTF to pristine HATCN. The measured electrical conductivity of thin films depends in a highly non-monotonic manner on the composition of the mixture and shows significantly improved charge transport compared to the pristine films. The temperature-dependent conductivity, charge carrier concentration, and mobility were investigated across these compositions. Surprisingly, all compositions exhibited n-type behavior, except for pristine DBTTF. This behavior is explained by the electronic structure of the mixtures, as revealed by ultraviolet photoelectron spectroscopy, which indicates that charge injection and transport occur via the lowest unoccupied molecular orbital of the DAC and HATCN. Additionally, the observed electrical conductivity is strongly influenced by the morphology and structural ordering of the films. These findings offer valuable insights for the design of advanced materials with enhanced electrical performance.

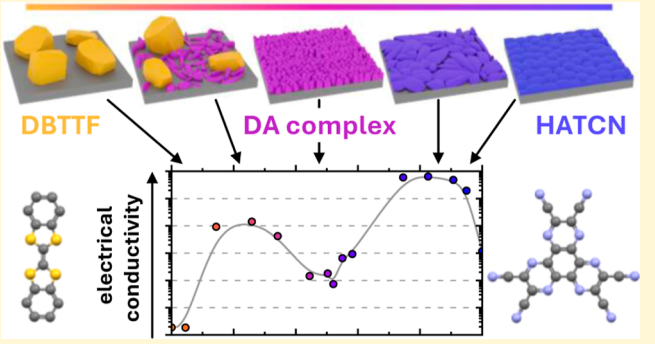

INTRODUCTION

The prospect of flexible and low-cost electronic devices made from organic semiconductors has attracted huge research interest. However, their application is limited due to, inter alia, typically lower charge carrier density and charge carrier mobility in comparison with those of inorganic semiconductors. The concept of charge-transfer doping has been developed to improve electrical conductivity by using strong electron donors and acceptors as dopants for organic semiconducting materials.[1−3] Strong dopants typically cause a complete (or at least partial) transfer of electronic charge from one molecular species to the other, with its propensity depending on the energy landscape as well as the structural arrangement.[4−6] To facilitate the transfer of charge between donor and acceptor, the ionization energy of the donor should be less than (or at least close to) the electron affinity of the acceptor, leading to ionization of both species, which is commonly termed integer charge transfer (ICT).[7] On the other hand, when the distance between donor and acceptor molecules is sufficiently close enough to allow for overlap of their π-orbitals due to a strong van der Waals interaction, orbital hybridization can occur, forming an electron donor−acceptor complex (DAC)[8] often without noticeable charge transfer.[9,10] In both cases, the strong interaction between donor and acceptor molecules leads to optical absorption features below the energy gaps of the pristine materials.

While the case of ICT has been extensively studied,[7] doping by DAC formation and its effect on electrical conduction is by far less investigated,[11,12] although it is the key to improving the performance of organic semiconductor devices. It can not only lead to an improvement in electrical conductivity but can also form different crystalline phases with a lower band gap and may be intermixed with the excess donor or acceptor molecules leading to a complex phase behavior of such blends.[12−14] To achieve high electric conductivity, high doping efficiency is required, and the produced electron−hole charge carrier pairs need to overcome their mutual Coulomb

Received: January 28, 2026
Revised: April 13, 2026
Accepted: April 17, 2026
Published: April 23, 2026

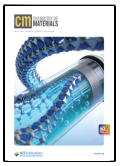

attraction to become mobile. A suited approach relies on using strong dopants to generate ICT states with high charge carrier density,[15] even though the doping efficiency in organic semiconductors has a limitation due to clustering or crystallite formation, resulting in a high thermal activation energy.[11,16]

Furthermore, a large activation energy has been reported at low doping concentration due to the presence of deep traps,[17,18] and deep Coulomb potentials caused by the interaction of mobile carriers with the ionized dopants.[19] On the other hand, as the doping concentration increases, π-orbitals begin to overlap, weakening the Coulomb force and reducing thermal activation energy.[20−23] In addition, it has recently been shown that dielectric screening becomes more effective, since the dielectric constant of doped organic semiconductors increases with doping concentration.[24,25]

In this paper, we combine the strong electron donor DBTTF, Dibenzotetrathiafulvalene,[26−29] with the strong acceptor HATCN, Hexaazatriphenylenehexacarbonitrile.[30−33] Both are rigid planar molecules which usually supports DAC formation, however, with significant differences in molecular shape and size.[34,35] Figure 1a shows the chemical structures of

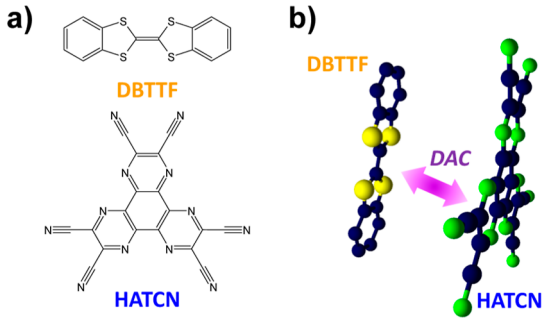

Figure 1. (a) Chemical structures of DBTTF (electron donor) and HATCN (electron acceptor). (b) Possible formation of a donor−acceptor complex (DAC) by mutually overlapping π-orbitals in a face-to-face arrangement.

both materials. Here, we fabricate films by coevaporation of both species from independently controlled sources with varying mixing ratios and study the formation of DACs between them (see Figure 1b), as well as their effect on electronic properties and electrical transport. For this, we apply a recently developed high-throughput thin film preparation technique to perform a seamless composition gradient between both materials[36] and study their structural, morphological, and optical characteristics to identify signatures of the emerging DAC phase. Thereafter, we fabricated a representative set of samples with different compositions on device-relevant substrates and studied their electronic structure and electrical transport properties. Depending on the mixing ratio, we find a wide range of different surface morphologies of codeposited thin films. Additionally, the occurrence of DACs changes the electronic characteristics and, specifically, reduces the activation energy for charge carrier generation, thus increasing the density of mobile charges and, with that, the electrical conductivity, as well.

RESULTS

A: Growth Studies

To study the structure, morphology, and the optical properties of the mixed DBTTF:HATCN films, we deposited a film with a compositional gradient along the substrate surface using a specially designed high-vacuum organic molecular beam deposition chamber.[36] The film with the nominal thickness of 20 nm was deposited on a silicon substrate (10×52 mm^2) with a native silicon oxide layer and had a compositional gradient along the long substrate direction. Probing different points on the sample surface with spatially resolved techniques, such as X-ray reflectometry (XRR), grazing-incidence wide-angle X-ray scattering (GIWAXS), atomic force microscopy (AFM), and UV−vis spectroscopy, allowed us to directly correlate the observed properties with the composition at the given position on the substrate. The details of the measurements are given in the Methods section.

Crystalline Structure. The evolution of the crystalline structure of the mixed gradient film as a function of composition was investigated with GIWAXS. GIWAXS measurements were performed at the ID10-SURF beamline of the ESRF-EBS synchrotron (Grenoble, France). Measurements were taken every 1 mm along the compositional gradient of the film. Figure 2a−c shows the reciprocal space maps corresponding to the pristine DBTTF edge, the pristine HATCN edge, and the 1:1 mixed phase.

The reciprocal space map for the DBTTF-rich edge (Figure 2a) shows sharp Bragg peaks, indicative of a well-oriented crystalline structure. The Bragg peak positions correspond to the previously reported crystalline structure of DBTTF in thin films[12] with a triclinic unit cell containing two DBTTF molecules with the unit cell parameters of a = 6.02 Å, b = 8.05 Å, c = 13.90 Å, α = 100.291°, β = 99.901°, and γ = 94.001° and the (001) plane parallel to the substrate. The peaks are split in the vertical direction, indicating that DBTTF does not form a continuous film.

In contrast, at the HATCN-rich edge (Figure 2c), the diffraction pattern contains several Debye−Scherrer rings. The q-positions of the observed Debye−Scherrer rings correspond to a large trigonal unit cell containing 18 HATCN molecules with the parameters $a = b$ = 23.8 Å, c = 15.1 Å, $\alpha = \gamma$ = 90°, and β = 120°.[37] The intensity distribution of the Debye−Scherrer rings in the azimuthal direction is almost uniform but has some modulations. These modulations can be attributed to a very weak preferred orientation of the (001) plane parallel to the substrate.

The mixed film exhibits Bragg peaks that are absent in the patterns of the pristine materials. At approximately 40−50 mol % of DBTTF content, the diffraction pattern contains only the cocrystal Bragg peaks, while the peaks associated with the pristine components completely disappear (Figure 2b). This suggests the formation of a mixed DBTTF:HATCN crystalline phase. The peaks are much broader than those of the pristine DBTTF phase in both directions, indicating a smaller crystallite size and a lower degree of orientation. So far, we have not been able to resolve the crystal structure of the cocrystal phase; however, it is different from known published structures of DBTTF:HATCN cocrystals grown by vapor-phase transport or from solution.[38] Crystals grown by vapor transport show a 3:2 stoichiometry, while all polymorphs grown by solvent evaporation have solvent molecules incorporated. However, since the cocrystal structure is dominant at 1:1 mixing ratios, we assume that this molecular ratio is also present in the unit cell.

The diffraction patterns at other positions and mixing ratios can be described as a linear combination of these three characteristic patterns. We quantified the evolution of the

https://doi.org/10.1021/acs.chemmater.6c00277
Chem. Mater. 2026, 38, 4726−4737

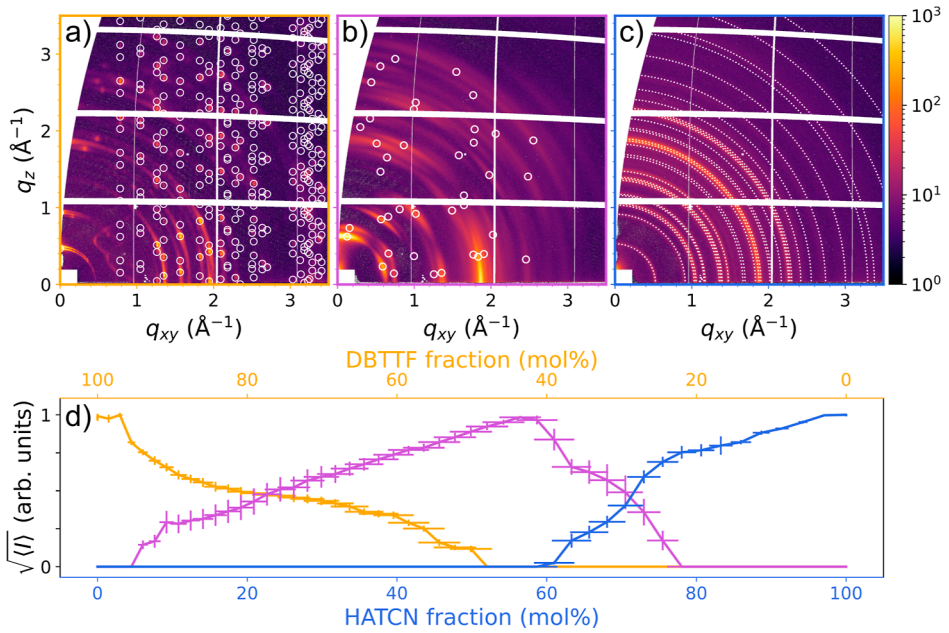

Figure 2. Crystalline structure of the DBTTF:HATCN film with gradient in relative concentrations. (a–c) Reciprocal space maps measured at the DBTTF edge (a), HATCN edge (c), and in the mixed part of the sample (b). Arcs and circles indicate the simulated peak positions for the previously reported structures of the pristine DBTTF and HATCN phases and the fitted peak positions for the mixed phase. (d) Square root of the average fitted intensity of selected Bragg peaks corresponding to the crystalline phases shown in panels (a–c). The intensity corresponding to the pristine DBTTF phase is shown in orange, the pristine HATCN in blue, and the mixed phase in purple.

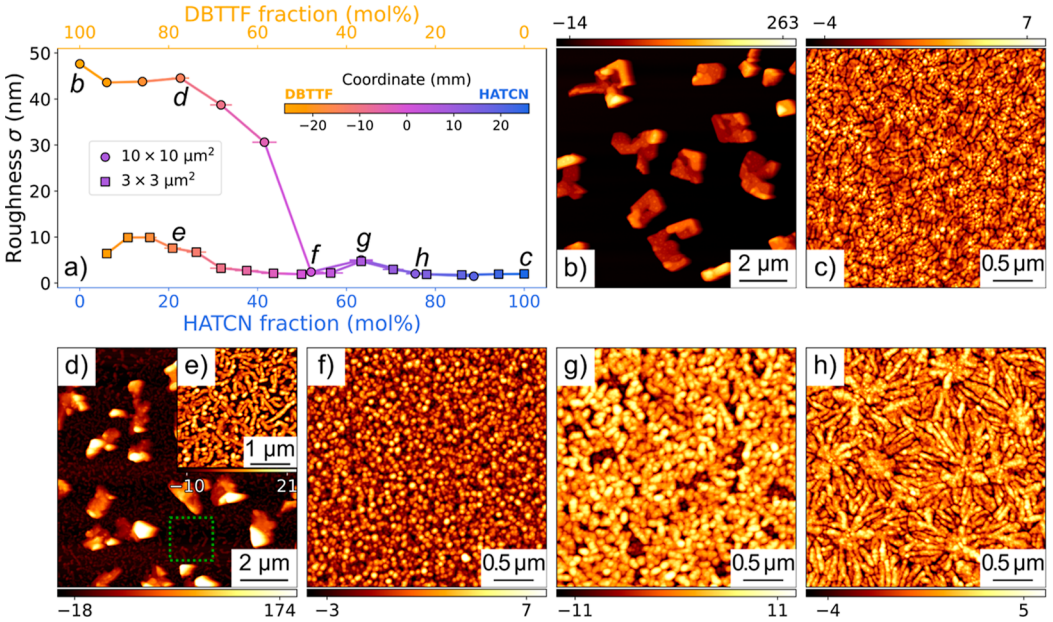

Figure 3. Morphology of the DBTTF:HATCN gradient film. (a) Roughness values extracted from AFM scans at different spatial positions along the gradient. The upper curve (circles) is extracted from large (10×10 μm^2) scans, and the bottom (squares) one from smaller (3×3 μm^2) scans between large particles. The letters next to the curves denote the positions where the AFM maps in (b–h) were measured. (b,c) AFM maps of pristine DBTTF (b) and HATCN (c) measured at the edges of the gradient sample. (d–h) AFM maps measured at different positions in the mixed part of the film. Inset (e) shows a smaller scan measured between the large particles as shown in (d) with a green square. The zero value corresponds to the mean height value for each map.

crystalline structure by fitting the 5 to 10 most intense Bragg peaks of each observed crystalline phase in every measured pattern. The average intensity of the Bragg peaks is approximately proportional to the volume squared of the corresponding crystalline phase.[39] The square root of the averaged Bragg peak intensity, shown in Figure 2d, is therefore approximately proportional to the volume fraction of the three crystalline phases described above.

Starting from pristine DBTTF, the intensity of the DBTTF Bragg peaks remains almost constant up to approximately 5 mol % of HATCN content. At this concentration, the intensity of the DBTTF Bragg peaks starts to decrease significantly, while peaks corresponding to the mixed DBTTF:HATCN

https://doi.org/10.1021/acs.chemmater.6c00277
Chem. Mater. 2026, 38, 4726–4737

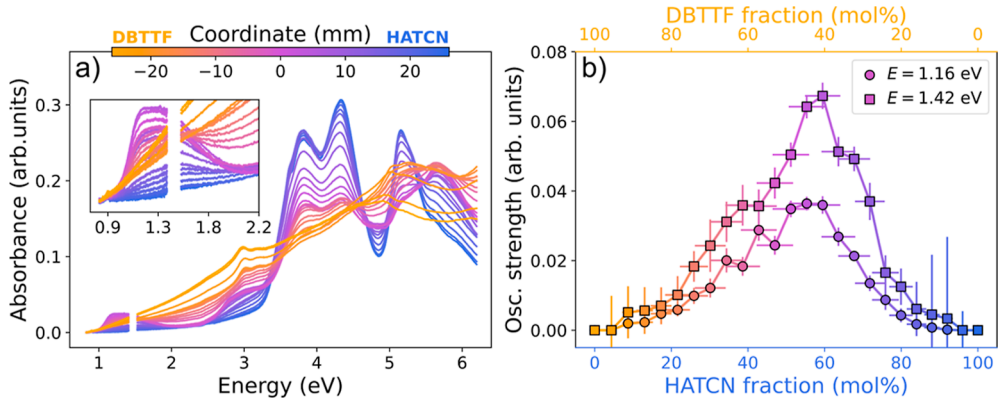

Figure 4. (a) UV−vis absorption spectra of the DBTTF:HATCN gradient film. The inset highlights the low-energy region of the spectra, where the CT absorption peak is located. The curves are color-coded according to the position along the film, as indicated by the color bar. (b) Extracted oscillator strength for the two CT absorption peaks at 1.16 eV (circles) and 1.42 eV (squares).

phase appear. The volume fraction of the mixed phase increases almost linearly within the range of 10−55 mol % HATCN content. The maximum intensity of the corresponding Bragg peaks at approximately 55 mol % coincides with the disappearance of the DBTTF-related peaks. Within the narrow range of 50−60 mol % HATCN content, only peaks characteristic of the mixed phase are present. This indicates 100 mol % conversion into the cocrystalline structure in this compositional range. At 60 mol % of HATCN content, the Debye−Scherrer rings originating from the HATCN phase appear. As the HATCN content increases further, the mixed phase quickly disappears at around 80 mol %. Interestingly, the HATCN-related rings continue to increase in intensity within the 80−95 mol % HATCN content range. We suggest that a small amount of smaller DBTTF molecules in this region can admix to the crystals with larger HATCN molecules, decreasing their crystalline order without substantially changing the structure.

Film Morphology. Generally, the roughness and morphology evolution in two-component systems exhibits rather rich behavior.[40] The morphological change in real space across the DBTTF:HATCN thin film is shown in Figure 3. Figure 3a shows the root-mean-square (RMS) roughness extracted from AFM images acquired at different positions along the compositional gradient. The dependence has two regimes in the DBTTF-rich region due to the coexistence of small and large DBTTF agglomerates, as will be discussed below. The upper region shows the values extracted from large AFM maps including the large prominent islands, and the lower shows the values from smaller maps measured between the large particles. Additional measurements of the roughness evolution with composition by means of XRR are given in the Supporting Information and support the results shown here.

Figure 3b shows an AFM map measured in the pristine DBTTF region of the gradient film. DBTTF does not form a continuous film; instead, we observe large regularly shaped particles approximately 100 nm in height and 1 μm in width, typical of pristine DBTTF films grown on native silicon oxide.[29] In contrast, at the HATCN-rich edge shown in Figure 3c, we observe a continuous film with an RMS roughness of 1.5 nm, where irregular fine grains with the characteristic lateral size of 330 nm are observed, typical of pristine HATCN films.[41]

The mixed region of the film shows a wide range of different morphological features. As the HATCN content increases, the large, nonpercolating crystallites characteristic of pristine DBTTF become more irregular in shape (Figure 3d) but remain present. At the same time, within the intergranular regions between the large islands, we observe smaller elongated crystallites with characteristic lengths of ∼350 nm (Figure 3e). We speculate that the small crystallites in this region consist of the mixed DBTTF:HATCN phase, while the large crystallites contain mostly the excess DBTTF phase. This speculation is further supported by Raman mapping performed in this sample region, where the large crystallites are proven to contain more DBTTF (see Supporting Information). The coexistence of large DBTTF-rich and small cocrystallites is characteristic of the entire DBTTF-rich part of the sample up to a molar fraction of about 0.5. In this region, spherical grains with a diameter of ∼50 nm form a continuous film with the lowest roughness of ∼1 nm. With increasing HATCN content, the roughness reaches a local maximum of approximately 5 nm at 0.6−0.7 HATCN molar fraction (Figure 3g), where the morphology changes toward the formation of larger spherical crystallites with the characteristic size of ∼80 nm. With a further increase in HATCN content, elongated spherulite-like grain structures emerge (Figure 3c). The typical length of the elongated particles here reaches a diameter of about 300 nm, while the roughness decreases down to ∼1 nm.

Morphology and chemical distribution were additionally studied by using Photoinduced Force Microscopy (PiFM)—a nanoscale imaging and spectroscopy technique that combines atomic force microscopy (AFM) with infrared (IR) spectroscopy to map chemical compositions with a spatial resolution better than 10 nm. These results confirm the discussion presented above and are given in detail in Supporting Information.

Optical Properties. The optical absorption in the ultraviolet, visible, and near-infrared (UV−vis−NIR) spectral range of the DBTTF:HATCN gradient film measured at 2 mm intervals (corresponding to steps of ∼4 mol % in composition) along the compositional gradient is shown in Figure 4a. The spectrum corresponding to the DBTTF edge is dominated by scattering rather than absorption since DBTTF does not form a continuous film but larger isolated islands, as shown by AFM. However, two weak, yet distinguishable absorption peaks at ca. 3.0 eV and ca. 5 eV can be recognized. The peak positions and the spectral profile are in agreement with previous studies.[34,42] At the HATCN edge, distinct absorption peaks are observed at 3.81, 4.33, and 5.16 eV. The peak at 3.81 eV corresponds to

https://doi.org/10.1021/acs.chemmater.6c00277
Chem. Mater. 2026, 38, 4726−4737

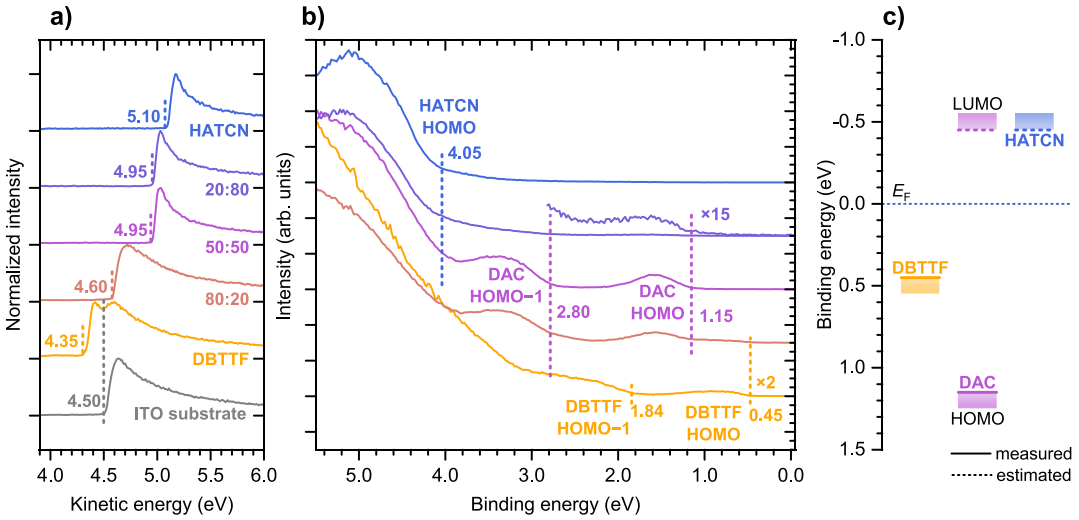

Figure 5. (a) Secondary electron-cutoff (SECO) and (b) valence spectra measured for the ITO substrate (only SECO), the pristine films, and 3 mixed films. (c) Energy-level diagram of frontier orbitals deduced from SECO and valence spectra (for details, see the text). The mixing fractions are given in mol %.

the lowest-energy optical transition of HATCN in accordance with previous studies.[43]

The inset in Figure 4a shows a magnified view of the low-energy region (0.8−2.2 eV) of the spectra, where a broad absorption peak emerges in the middle of the composition gradient. This broad peak is indicative of DAC formation between the two molecular components. The peak was fitted with two Tauc−Lorentz oscillators with transition energies of (1.16 ± 0.01) eV and (1.42 ± 0.04) eV. The emergence of fine structure in this region may be associated with a Davydov splitting.[44] The peak positions do not change substantially with variations in the composition. The extracted oscillator strengths for these two transitions are shown in Figure 4b, as a function of the molar fraction of the two materials. A maximum strength for both transitions is reached at a DBTTF:HATCN ratio of approximately 1:1, corresponding to the region of the strongest CT absorption. We note that another optical transition emerges at approximately 3 eV in the mixed region of the film and demonstrates the same behavior.

B: Device Studies

For device studies, we grew a series of distinct samples on substrates with electrode structures for different types of measurements. These were ITO-covered glass substrates for photoelectron spectroscopy, as well as glass substrates with patterned ITO finger electrodes for electrical conductivity measurements. For field-effect transistor structures, we used Si wafers with thermal oxide and an additional poly(methyl methacrylate) passivation layer. Most importantly, these samples were grown at higher deposition rates of 0.4− 0.6 Å/s but without air exposure between growth and measurements. In the Supporting Information (see Figure S4), we show exemplary AFM images of such samples to verify that film morphologies were comparable to the gradient samples used for growth studies. We want to note that due to the large difference in growth rate, some minor differences occur in the individual film morphologies, but the overall behavior is qualitatively similar.

Electronic Structure. The valence energy levels (i.e., the highest occupied molecular orbitals, HOMOs) and secondary electron cutoff (SECO) of pristine and mixed thin films (DBTTF-rich—4:1, equimolar—1:1, HATCN-rich—1:4) were measured by ultraviolet photoelectron spectroscopy (UPS) to understand the electronic structure and the energy level alignment on ITO electrodes. The samples were fabricated by depositing 25 nm of organic material on ITO-coated glass substrates. The obtained data is shown in Figure 5a. The work function of the clean ITO substrate is about 4.5 eV as determined from the onset of its SECO. This value is within the usual range of UPS measurements.[45] Additionally, a reduction of work function might appear on the ITO sample with contamination due to the pushback effect.[46,47] Depositing pristine DBTTF on ITO results in a double SECO, which underlines the incomplete coverage as discussed in the film morphology section. The lower SECO onset represents the DBTTF work function of 4.35 eV, and the second feature is related to the work function of the ITO substrate, which can be observed due to the pronounced island growth of the DBTTF film. The reduction of work function in the DBTTF region is ascribed to HOMO pinning of the DBTTF at the Fermi level of the ITO, which is induced by charge transfer between the organic material and the electrode.[48] In contrast, the SECO shift to higher kinetic energies after the deposition of pristine HATCN on ITO is induced by pinning at the HATCN LUMO level.[49,50] The resulting work function in this case is 5.10 eV. The work functions of the mixed films are found between these extreme cases of pristine materials. The equimolar film and the HATCN-rich film exhibit almost the same value of the work function of 4.95 eV, and the work function of the DBTTF-rich film (4.60 eV) is closer to that of pristine DBTTF.

Figure 5b shows the photoelectron spectrum of the occupied valence states for the pristine and mixed films. The HATCN film shows the HOMO onset energy of 4.05 eV, which agrees with the LUMO pinning concluded from the SECO measurements.[31] The DBTTF film exhibits clearly separated HOMO and HOMO-1 states. The HOMO of DBTTF is pinned at the Fermi level, as concluded before from SECO reduction. As the surface is inhomogeneously covered with molecules, the ionization energy differs from reports in the literature.[51,52] Same DBTTF features are weakly observed for the DBTTF-rich film (not shown). However, two features with onsets at

https://doi.org/10.1021/acs.chemmater.6c00277
Chem. Mater. 2026, 38, 4726−4737

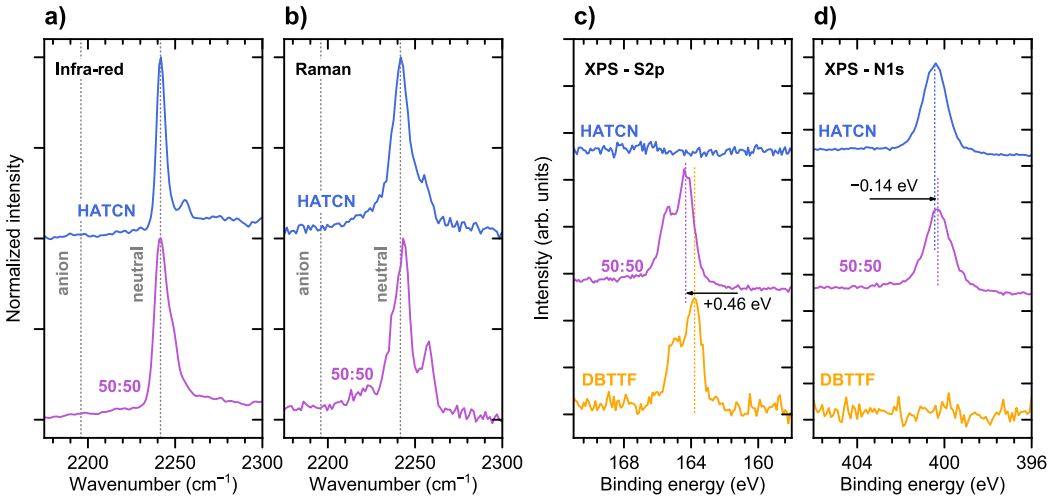

Figure 6. (a) FTIR (in transmission) and (b) Raman spectra of a HATCN and a DBTTF:HATCN equimolar mixed film in the wavenumber range of the C≡N vibration. The mixing fractions are given in mol %. The mode in the neutral (2241 cm^{-1}) and in the anionic (2196 cm^{-1}) state of the HATCN molecule is taken from the literature.[32] The X-ray photoelectron spectra (XPS) of (c) S 2p and (d) N 1s peaks for DBTTF, HATCN, and the equimolar mixed thin film. The arrows indicate the peak shift from the respective peak in the pristine film to the equimolar mixed film.

1.15 and 2.80 eV are much more prominent, which are present exclusively in the mixed films. This fact points toward the formation of states that are present only when the two molecular orbitals hybridize and form a DAC. Thus, these features are attributed to HOMO and HOMO-1 of the DAC. The spectrum of the HATCN-rich film has strong resemblance with the pristine HATCN film with the addition of weak DAC features. Also, the HATCN HOMO onset is present at the same energy as that in the pristine HATCN film. These data are in agreement with phase separation in the nonequimolar films between the DAC and the excess material (DBTTF or HATCN), observed by X-ray scattering and optical spectroscopy. Taking the HOMO onset of the DAC at 1.15 eV and the optical gap of 1.16 eV (transition energy of the first Tauc–Lorentz oscillator), the LUMO of the DAC is located at the value of the exciton binding energy above the Fermi level. Exciton binding energy is given in the range of several 100 meV.[53,54] This low energy distance between Fermi energy and LUMO position is in accordance with LUMO pinning of the DAC as concluded from the SECO increase mentioned before.

The resulting energies of the HOMO onset determined from photoelectron spectroscopy measurements and estimated LUMO values are summarized in Figure 5c. For simplification, the same pinning level of 0.45 eV for DBTTFs HOMO is used also for the LUMO pinning of DAC and HATCN, as the LUMO pinning levels can only be estimated here. This results in a much lower electron than hole injection barrier for the DAC as well as an "n-type" positioning of E_F within the energy gap of the complex, which will become relevant for electrical transport later.

Degree of Charge Transfer. Clear evidence of the formation of an electron donor–acceptor complex in the mixed DBTTF:HATCN films has been obtained from optical absorption and UPS measurements. Here, we analyze the degree of charge transfer from the energy position of the C≡N vibrational mode as well as from the composition of the molecule-specific core electron levels measured by X-ray photoelectron spectroscopy.[55−57]

Fourier-transform infrared (FTIR) and Raman spectra of a pristine HATCN film and an equimolar DBTTF:HATCN mixed film are shown in Figure 6a,b, respectively. The neutral HATCN shows an intense Raman band corresponding to the vibrational mode of the C≡N group at 2241 cm^{-1}.[32] This band is barely shifted for the DBTTF:HATCN mixture. Also, no significantly shifted additional feature is detectable. However, the relative intensity and position of the high energy shoulder are altered in the mixed film compared with the pristine HATCN film. This shows a clear difference in the respective local HATCN environments within these two films. Given a reported shift of the vibrational mode by 45 cm^{-1} when going from neutral HATCN to anionic HATCN molecules,[32] the degree of CT in the DBTTF:HATCN DAC is therefore negligible if a linear relationship between frequency shift and degree of charge transfer is assumed.[55]

The chemical composition of the sample surface was characterized by using X-ray photoelectron spectroscopy (XPS). Here, the sulfur 2p and nitrogen 1s orbitals are fingerprints for DBTTF and HATCN, respectively. Figure 6c,d shows the core-level energy region of the S 2p and N 1s peaks. Going from pristine films to the equimolar mixed film, the S 2p peak shifts to higher energies and the N 1s peak to lower energies by +0.46 eV and −0.14 eV, respectively. This is in accordance with the shifts of the DBTTF HOMO and HATCN LUMO levels upon forming HOMO and LUMO levels of the complex. A detailed deconvolution of the XPS data is given in Supporting Information. In short, the S 2p peak consists of the $2p_{3/2}$ and the $2p_{1/2}$ features, while the N 1s peak comprises two features of different bonding environments of nitrogen in HATCN, viz., the different N atoms in the ring and in the cyano groups. Furthermore, both HATCN spectra show a second component shifted to lower binding energies indicating the anionic HATCN species.[31] As there is no equivalent cationic species found in S 2p spectra of DBTTF, these features are related to charge transfer between HATCN molecules and the substrate, which leads to the Fermi-level pinning. This effect is much more pronounced for HATCN than for DBTTF films, as shown by the larger SECO shift for HATCN than for DBTTF. Consequently, the intermolecular CT between DBTTF and HATCN is negligible, in agreement with the results from vibrational spectroscopy. Note that, in general, the degree of CT in donor–acceptor cocrystals varies between different polymorphs, and zero degree of CT was also

https://doi.org/10.1021/acs.chemmater.6c00277
Chem. Mater. 2026, 38, 4726−4737

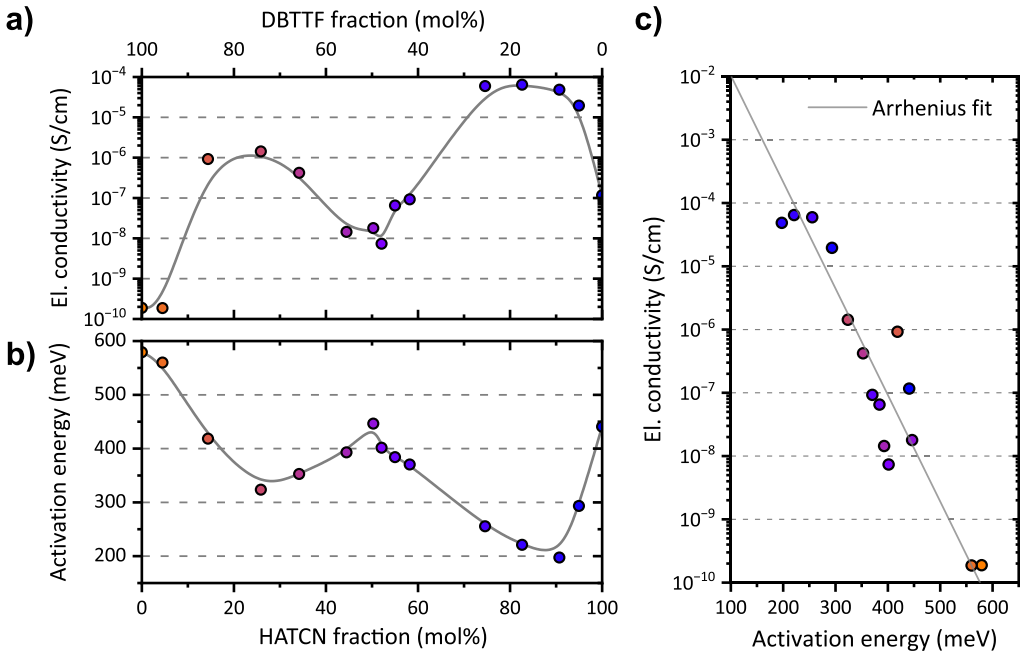

Figure 7. (a) Electrical conductivity (at room temperature) and (b) thermal activation energy (from temperature-dependent conductivity measurements) across the entire range of DBTTF:HATCN concentrations. The data exhibit an inverse relationship between electrical conductivity and activation energy, consistent with the Arrhenius model. (c) The room-temperature conductivity data are fitted using the Arrhenius equation, eq 1, yielding a prefactor σ_0 = 1.2 S/cm.

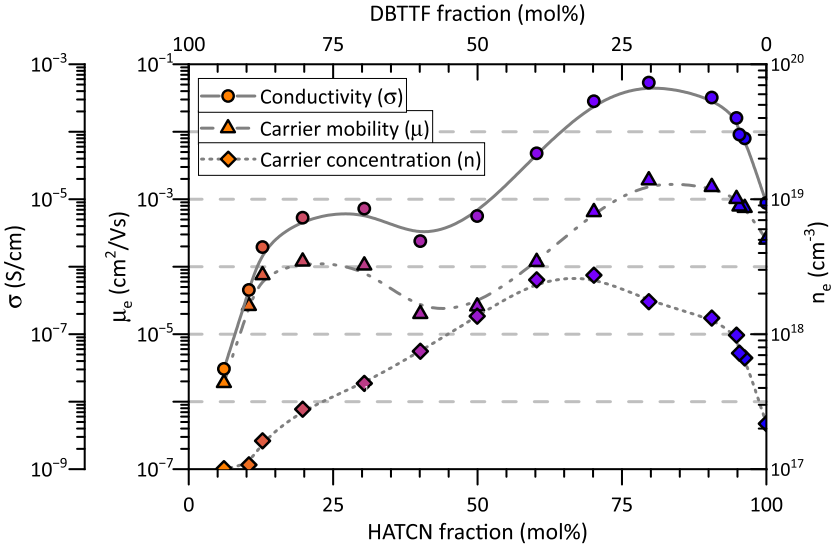

Figure 8. Charge carrier mobility (μ) and carrier concentration (n) in DBTTF:HATCN thin films were extracted from field-effect transistor measurements and from Mott−Schottky analysis on MIS diodes. In both experimental approaches, only negative charge carriers could be detected. The product of both quantities yields the electrical conductivity (σ).

observed for other systems, like DBTTF:TCNQ and DBTTF:TCNNQ.[10,58]

Electrical Conductivity. The electrical conductivity of organic semiconductors is often governed by hopping transport, wherein the conductivity exhibits a strong temperature dependence, displaying thermally activated behavior, as described by the Arrhenius model (eq 1). This behavior is characterized by a material-specific activation energy E_a and a prefactor σ_0, which represents the conductivity limit at an idealized infinite temperature.

$$\sigma(T) = \sigma_0 \times \exp\left(-\frac{E_a}{k_B T}\right) \quad (1)$$

Note that this equation can be used in a 2-fold manner: First, the activation energy of a given sample was extracted from its temperature-dependent electrical conductivity, yielding values of E_a and σ_0 for each different composition. And, second, to compile a systematic relation between the conductivities of different samples at a given temperature, e.g., σ(300 K), and their activation energies, as will be discussed below.

Improving electrical conductivity necessitates either a reduction in activation energy E_a or an enhancement of σ_0.

https://doi.org/10.1021/acs.chemmater.6c00277
Chem. Mater. 2026, 38, 4726−4737

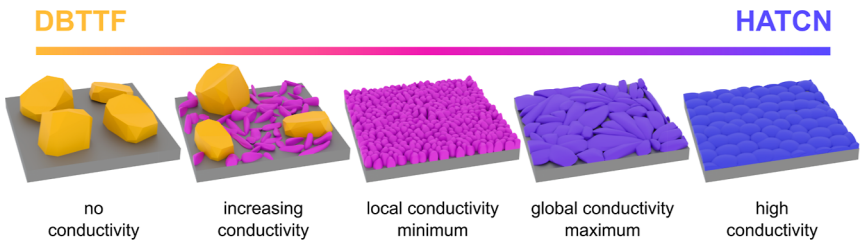

Figure 9. Sketch of the phase behavior of DBTTF:HATCN mixtures and the implications for charge transport along the composition gradient from pristine DBTTF (left) to pristine HATCN (right). DBTTF crystallites are shown in dark yellow, the DAC in purple, and HATCN in dark blue. Further details are given in the text.

Recent findings indicate that a broad range of doped organic semiconductors with integer charge transfer adhere to this model at room temperature (T = 300 K), with a common σ_0 value around 15 S/cm, while activation energies range from 40 to 400 meV.[7]

To investigate the behavior of DBTTF:HATCN within this context, we prepared 15 distinct mixtures of the two materials, including pristine films of each species. Figure 7 illustrates the room-temperature conductivities and thermal activation energies across the entire mixing range. Detailed Arrhenius fit parameters for all samples are provided in Table S1 in the Supporting Information.

Notably, the electrical conductivity of DBTTF:HATCN mixtures at 300 K (Figure 7a) reveals two maxima at approximately 25 and 80 mol % HATCN. Correspondingly, there are two minima in activation energy (Figure 7b), with the lowest value of about 200 meV observed at 80−90 mol % HATCN. Interestingly, the equimolar DBTTF:HATCN mixture exhibits a local conductivity minimum and an activation energy maximum. It should be noted that pristine DBTTF (and the 95 mol % DBTTF films) has extremely low conductivity, attributed to noncontinuous film formation, leading to island growth as evidenced by AFM imaging.

Figure 7c presents the room temperature conductivity plotted against thermal activation energy for all samples. Despite some scattering, the data appear to be consistent to the Arrhenius equation, as indicated by the fitted linear trend. This means that, similar to the case of ICT,[7] there is a correlation between room temperature conductivity and activation energy in these samples. However, the temperature independent prefactor σ_0 obtained from the fit is somewhat lower (1.2 S/cm) than that for ICT. This could indicate a lower doping efficiency in DBTTF:HATCN.

In addition to direct conductivity measurements, we also determined charge carrier mobility (μ) from organic field-effect transistor (OFET) characteristics as well as carrier density (n) and carrier type from Mott−Schottky analysis on metal−insulator−semiconductor (MIS) diodes. The raw data are presented in Figure S6 in the Supporting Information, while the extracted mobility and carrier density values are displayed in Figure 8. Due to morphological constraints, pristine DBTTF films were not measurable. Remarkably, all samples display n-type conductivity behavior because only electron accumulation was detected in both device types. The carrier concentration is peaking at approximately 60−70 mol % HATCN content. At the same time, carrier mobility in DBTTF:HATCN thin films exhibits a double maximum at around 20 and 80 mol % of HATCN, with a local minimum at the equimolar mixing ratio. As per the relationship $\sigma = qn_e\mu_e$, where q is the elementary charge, we calculated the resulting electrical conductivity. This calculated conductivity mirrors the experimental values, albeit with less variability and a less pronounced minimum in the range of equimolar mixtures. It is important to note that OFET and MIS diode measurements assess orthogonal sample directions (in-plane and out-of-plane, respectively), which could account for discrepancies with direct in-plane conductivity measurements. Additionally, the top-contact configuration employed in the measurements of charge carrier concentration and mobility may introduce differences in contact resistance and anisotropic mobilities compared with the bottom-contact setup used in direct electrical conductivity measurements. Nevertheless, the agreement with direct conductivity measurements shown in Figure 7a is very good.

The CT absorption band allows for a photoinduced conductivity increase under IR light illumination. The photoconductivity of the equimolar mixture was tested by excitation within the CT absorption band by using IR light at 850 nm. An improvement in charge carrier transport and injection was observed. Details are given in Supporting Information. Extended studies on photoconductivity have to be performed in the future to check sensitivity and response time.

DISCUSSION

The classification of organic semiconducting materials as donors or acceptors relies mostly on their relative energy levels. Typically, doping of one species by the other is performed by adding small amounts (1−10%) of a strong acceptor to a donor matrix to achieve p-type doping or vice versa for n-type doping. Here, we vary the mixing ratio of such a donor−acceptor system over the whole composition range from the pristine donor (DBTTF) to the pristine acceptor (HATCN) and study its phase behavior as well as the implications on the charge transport of such mixtures.

While we would, a priori, expect a (more or less) symmetric behavior between the donor-rich (p-doped) side and the acceptor-rich (n-doped) side, a strong asymmetry is found in the studied case of DBTTF:HATCN. Specifically, pristine DBTTF shows very low (or almost negligible) electrical conductivity, while high conductivities are found on the HATCN-rich side (Figure 7a). Moreover, except for the pristine DBTTF, all compositions show n-type conduction. However, the increase of conductivity from the donor-rich to the acceptor-rich side is nonmonotonic but shows a pronounced conductivity minimum at around equimolar composition.

To account for this unexpected behavior, we have performed a comprehensive series of experiments combining film growth and device studies to elucidate the phase behavior of the

https://doi.org/10.1021/acs.chemmater.6c00277
Chem. Mater. 2026, 38, 4726−4737

mixtures and relate it to the observed electrical transport. This is schematically shown in Figure 9. In particular, film structure and morphology studies indicate that pristine DBTTF forms large almost nonpercolating crystallites, which persist over the entire DBTTF-rich side of the composition range and lead to considerable film roughness, whereas the HATCN-rich side exhibits very smooth films without pronounced signs of phase separation (Figure 3). Most importantly, however, apart from the known pristine DBTTF and HATCN crystal structures, we find a distinctly different crystal structure around the equimolar mixing ratio of both components, which we assign to a donor−acceptor complex (Figure 2). This is corroborated by optical absorption spectra that unequivocally reveal the appearance of an absorption feature at about 1.3−1.4 eV below the absorption edges of the two pristine materials, which is a clear fingerprint of a charge-transfer state formed by the electronic interaction between the DBTTF donor and the HATCN acceptor (Figure 4).

Photoelectron spectroscopy further manifests this view (Figure 5). The DAC exhibits two clearly separated occupied states, which we assign to HOMO and HOMO-1 of the complex. Their formation can be envisioned by hybridization between the respective occupied states of the donor DBTTF and the LUMO of HATCN. Importantly as for the latter, the LUMO of the DAC seems to be pinned at the same relative energy of −0.45 eV above the Fermi level of the ITO substrate, which may be seen as the real origin of the observed n-type conduction in all the mixtures, since the barrier for hole injection into the HOMO of the complex is way too high (>1.1 eV).

Interestingly, however, infrared/Raman as well as X-ray photoelectron spectroscopy do not indicate a substantial degree of ground-state charge transfer between DBTTF and HATCN in the formed DAC (Figure 6).[59] Nevertheless, we observe an increase in carrier density (Figure 8) from Schottky−Mott analysis on MIS diodes that is clearly correlated with the existence of the crystal structure of the DAC and its optical signature in UV-vis absorption. Note, the DAC cocrystals act as dopants here.[11] The carrier density peaks at about 60−70% HATCN, similar to the other two signatures, and can be clearly assigned to the formation of the DAC. Thus, even without noticeable CT between the donor and acceptor, the complex promotes the generation of mobile charge carriers, which is the prerequisite for an enhancement of electrical conductivity in the mixture.

What is, nonetheless, somewhat unexpected is that the electrical conductivity does not just follow the carrier density but exhibits a local minimum around the equimolar mixing ratio of DBTTF and HATCN, which is also reflected in a minimum of charge carrier mobility in this range (Figure 8). This "anomaly" seems to be related to film morphology, as evidenced by our AFM studies. Starting from pristine DBTTF with its pronounced island growth and very rough films (Figure 3h), the increasing amount of the DAC (growing as rather smooth "filler" between the DBTTF islands, Figure 3f,g) improves all electrical parameters, including carrier density and mobility, by forming a percolating crystalline network in between the DBTTF islands. However, as soon as the equimolar ratio is reached with the crystalline phase of DAC being the dominant species, the grain size shrinks and causes a very fine-grained film morphology with lots of grain boundaries (Figure 3e). We ascribe this change in film morphology, which is coupled to the prevalence of the DAC, to the main cause for the reduction in charge carrier mobility and electrical conductivity in equimolar mixtures. Additionally, a reduced electronic coupling between the DA molecules in the cocrystal structure might also reason the lower mobility and increased activation energy of DAC films compared to pristine and doped HATCN films.[60] The global maximum in electrical conduction is reached at about 70−90% HATCN content in the mixture because, in this range, film morphology exhibits crystalline needle-like structures (Figure 3h), which are favorable for charge transport. At the same time, the signature of DAC crystallites rapidly vanishes so that the remaining DACs are probably molecularly dispersed in the HATCN matrix, and the DAC cocrystals, as mentioned before, act as n-dopants.

Overall, electrical conductivity and its thermal activation show a similar behavior to that found for integer CT doping in a wide range of organic semiconductors (Figure 7c). It follows an Arrhenius law with a "universal" prefactor that is roughly by a factor of 10 smaller compared to the ICT case. This can be considered as an indicator for a lower doping efficiency in complex doping.[10,34]

CONCLUSION

We have studied the structural phase and mixing behavior of the organic molecular donor DBTTF and the acceptor HATCN. Using a dedicated codeposition technique, we were able to fabricate samples with a seamless composition gradient on a single substrate, which are used for high-throughput analysis of film properties. By correlating the obtained structural, morphological, and optical data with electrical and electronic device characteristics, we were able to identify the formation of a DAC with a distinctly different crystal structure and characteristic electronic signatures in the subgap region of the pristine materials. Electrical transport is affected in two ways by DAC formation: On the one hand, DACs increase carrier density, and their LUMO-level pinning leads to n-type conduction over almost the entire composition range. On the other hand, the prevalence of the DAC phase around equimolar composition is characterized by a fine-grained morphology with the abundance of grain boundaries, which in turn reduces the macroscopic charge carrier mobility and leads to a pronounced minimum in electrical conductivity at this composition.

Altogether, our comprehensive studies of the phase behavior of this DAC forming mixture provide detailed insights into its electrical transport and its correlation to morphology, which is the prerequisite for developing future materials with tailored electrical and optical properties, e.g., infrared photodetectors.

EXPERIMENTAL SECTION

Materials

Dibenzotetrathiafulvalene (DBTTF) was purchased from Sigma-Aldrich Chemie GmbH, and 1,4,5,8,9,11-Hexaazatriphenylenehexacarbonitrile (HATCN) was purchased from Ossila Ltd. The powders were used without further purification. Mixing fractions are given in mol % from $c_D/(c_D + c_A)$ or $c_A/(c_D + c_A)$.

A: Growth Studies

Film Growth. The gradient films were prepared by organic molecular beam deposition (OMBD) in a custom-designed chamber equipped with two independently controlled evaporation cells.[36] The films with the nominal thickness of 20 nm was simultaneously deposited on a silicon substrate (10 × 52 mm^2) with a native silicon oxide layer and on quartz glass. The composition varied along the

https://doi.org/10.1021/acs.chemmater.6c00277
Chem. Mater. 2026, 38, 4726−4737

long substrate axis. The deposition rate was equal to 2 Å/min, and the base pressure was about 10^{-8} mbar. The effective thickness was monitored during the film growth by a quartz crystal microbalance (QCM). The compositional gradient was achieved with a specially designed moving shutter composed of two synchronized steel blades oscillating along the gradient axis. The linear motion of the shutter produced a continuous gradient across the substrate. Further details are provided in ref 36.

Film Structure. Grazing-incidence wide-angle X-ray scattering (GIWAXS) measurements were performed at the ID10-SURF beamline at the ESRF (Grenoble, France). The X-ray beam with the energy of E = 18 keV (λ = 0.0689 Å) was focused down to the size of ~0.01 × 0.03 mm^2 (vert. × hor.). Measurements were taken every 1 mm along the compositional gradient of the film. Data processing and analysis were done using the pygid package,[61] including data conversion, background subtraction, and peak position simulation.

Film Morphology. The film morphology grown on a silicon substrate was characterized by atomic force microscopy (AFM) (JPK BioMAT workstation, JPK Instruments, now Bruker) with Budget-Sensors All-In-One cantilevers in tapping mode. Image processing was performed using Gwyddion software.[62]

Optical Spectra. Optical absorption spectroscopy was performed on samples grown on quartz glass by using a PerkinElmer Lambda 950 UV-vis spectrometer. Baseline correction was applied by using bare quartz glass. The gradient film was measured at 2 mm intervals along the compositional gradient axis.

B: Device Studies

Film Growth. For device studies, films were grown in a home-built high-vacuum organic molecular beam deposition chamber equipped with two independently controlled low-temperature effusion cells having separately monitored quartz-crystal balances. Organic films of both pristine materials and several mixtures with different mixing ratios were deposited at rates of 0.4−0.6 Å/s on ITO-covered glass substrates for photoelectron spectroscopy as well as on glass substrates with patterned ITO finger electrodes for electrical conductivity measurements. For field-effect transistor structures, we used Si wafers with a thermal oxide and an additional PMMA passivation layer. Film thicknesses were nominally around 50 nm (not including effects of film roughness etc.). Importantly, samples for device studies had never been exposed to ambient air between growth and measurement.

Photoelectron Spectroscopy. Photoelectron Spectroscopy was carried out in the Humboldt-Universität zu Berlin using the hemispherical electron analyzer SPECS Phoibos 100 with the He-discharge lamp as UV sources (excitation energy: 21.218 eV) for the valence region and a Mg K_α X-ray source (excitation energy: 1253.6 eV) for the core-level region. Secondary electron cutoff (SECO) measurements were conducted with a sample bias of −10 V. The setup resolutions are 100 meV for UPS referring to the width of the Fermi edge of Au and 900 meV for XPS referring to the width of the Au $4f_{7/2}$ peak.

Vibrational and Raman Spectroscopy. Samples were prepared on nondoped, double-side polished silicon wafers (Siegert prime grade, 1 mm thickness, native oxide, used as received). Fourier-transformed infrared (FTIR) spectroscopy was performed in vacuo using a Bruker IFS-66v spectrometer with a midrange mercury cadmium telluride detector cooled with liquid nitrogen. Raman spectroscopy was performed using an XploRA Plus confocal microscope (Horiba, Inc.) using an excitation wavelength of 532 nm.

Electrical Characterization. Temperature-dependent electrical conductivity measurements were performed with a semiconductor parameter analyzer (Keithley 4200A-SCS) under high vacuum in a CRYOVAC variable-temperature liquid nitrogen cryostat between room temperature and about 200 K. The same instrument was also used for electrical measurements on OFETs in the linear and saturation regime to extract carrier mobility. Impedance spectroscopy on MIS diodes was performed by using a Solartron 1260 Frequency Response Analyzer in combination with a Solartron 1296 Dielectric Interface.

■ ASSOCIATED CONTENT

Data Availability Statement

Data produced at the ID10-SURF beamline at ESRF (Grenoble, France) are available at https://doi.org/10.15151/ESRF-ES-1940867632.

Supporting Information

The Supporting Information is available free of charge at https://pubs.acs.org/doi/10.1021/acs.chemmater.6c00277.

Additional information on growth study, absorption, film morphology for devices, core level structure, electrical transport, and photoconductivity (PDF)

■ AUTHOR INFORMATION

Corresponding Authors

Andreas Opitz − *Institut für Physik, Humboldt-Universität zu Berlin, Berlin 12489, Germany;* orcid.org/0000-0002-3214-8398; Email: andreas.opitz@hu-berlin.de

Dmitry Lapkin − *Institut für Angewandte Physik, Universität Tübingen, Tübingen 72076, Germany;* orcid.org/0000-0003-0680-8740; Email: dmitry.lapkin@uni-tuebingen.de

Wolfgang Brütting − *Institut für Physik, Universität Augsburg, Augsburg 86159, Germany;* orcid.org/0000-0001-9895-8281; Email: wolfgang.bruetting@physik.uni-augsburg.de

Authors

Hongwon Kim − *Institut für Physik, Universität Augsburg, Augsburg 86159, Germany*

Gianfranco Melis − *Institut für Angewandte Physik, Universität Tübingen, Tübingen 72076, Germany;* orcid.org/0009-0005-2295-3608

Ainur Abukaev − *Institut für Angewandte Physik, Universität Tübingen, Tübingen 72076, Germany;* orcid.org/0000-0002-7164-5688

Marie Siegert − *Experimental Physics VI, Julius-Maximilians-Universität Würzburg, Würzburg 97074, Germany;* orcid.org/0000-0002-9058-8527

Lennart Frohloff − *Institut für Physik, Humboldt-Universität zu Berlin, Berlin 12489, Germany;* orcid.org/0000-0002-2178-0806

Lisa Schraut-May − *Experimental Physics VI, Julius-Maximilians-Universität Würzburg, Würzburg 97074, Germany;* orcid.org/0009-0004-0385-0753

Oleg Konovalov − *European Synchrotron Radiation Facility (ESRF), Grenoble 38043, France*

Alexander Hinderhofer − *Institut für Angewandte Physik, Universität Tübingen, Tübingen 72076, Germany;* orcid.org/0000-0001-8152-6386

Frank Schreiber − *Institut für Angewandte Physik, Universität Tübingen, Tübingen 72076, Germany;* orcid.org/0000-0003-3659-6718

Jens Pflaum − *Experimental Physics VI, Julius-Maximilians-Universität Würzburg, Würzburg 97074, Germany;* orcid.org/0000-0001-5326-8244

Complete contact information is available at: https://pubs.acs.org/10.1021/acs.chemmater.6c00277

Notes

The authors declare no competing financial interest.

https://doi.org/10.1021/acs.chemmater.6c00277
Chem. Mater. 2026, 38, 4726−4737

■ ACKNOWLEDGMENTS

Deutsche Forschungsgemeinschaft (project numbers 239543752 and 530008779) supported this work financially. This study is partially funded by the Federal Ministry of Education and Research (BMBF) and the Baden-Württemberg Ministry of Science as part of the Excellence Strategy of the German Federal and State Governments. We acknowledge the European Synchrotron Radiation Facility (ESRF) for provision of synchrotron radiation facilities under proposal number SC-5641. A.O. thanks Hanno Schroeder (HU Berlin) for sample preparation and testing. L.F. and M.S. gratefully acknowledge financial support from the German Environmental Foundation (Deutsche Bundesstiftung Umwelt, DBU). J.P. acknowledges financial support from the Bavarian State Ministry for Science and the Arts within the collaborative research network "Solar Technologies go Hybrid (SolTech)". L.S.-M. appreciates support from the Würzburg-Dresden Cluster of Excellence on Complexity and Topology in Quantum Matter, ct.qmat (EXC 2147). We would like to express our gratitude to Anfatec Instruments AG and, personally, Pranav Sudersan for the photoinduced force microscopy (PiFM) measurements presented in the Supporting Information.

■ REFERENCES

(1) Hase, H.; Salzmann, I. 11 - Doping in organic semiconductors. In *Handbook of Organic Materials for Electronic and Photonic Devices*, 2nd ed.; Ostroverkhova, O., Ed.; *Woodhead Publishing Series in Electronic and Optical Materials*; Woodhead Publishing, 2019; pp 349−383.

(2) Hofmann, A. I.; Kroon, R.; Müller, C. 13 - Doping and processing of organic semiconductors for plastic thermoelectrics. In *Handbook of Organic Materials for Electronic and Photonic Devices*, 2nd ed.; Ostroverkhova, O., Ed.; *Woodhead Publishing Series in Electronic and Optical Materials*; Woodhead Publishing, 2019; pp 429−449.

(3) Yuan, D.; Liu, W.; Zhu, X. Efficient and air-stable n-type doping in organic semiconductors. *Chem. Soc. Rev.* **2023**, *52*, 3842−3872.

(4) Brédas, J.-L.; Beljonne, D.; Coropceanu, V.; Cornil, J. Charge-transfer and energy-transfer processes in π-conjugated oligomers and polymers: a molecular picture. *Chem. Rev.* **2004**, *104*, 4971−5004.

(5) Theurer, C. P.; Richter, M.; Rana, D.; Duva, G.; Lepple, D.; Hinderhofer, A.; Schreiber, F.; Tegeder, P.; Broch, K. Coexistence of Ion Pairs and Charge-Transfer Complexes and Their Impact on Pentacene Singlet Fission. *J. Phys. Chem. C* **2021**, *125*, 23952−23959.

(6) Han, H.; Joo, B.; Kim, E.-G. Molecular electrical doping: One descriptor for any degree of charge transfer. *Synth. Met.* **2026**, *316*, 118018.

(7) Schwarze, M.; Gaul, C.; Scholz, R.; Bussolotti, F.; Hofacker, A.; Schellhammer, K.; Nell, B.; Naab, B.; Bao, Z.; Spoltore, D.; Vandewal, K.; Widmer, J.; Kera, S.; Ueno, N.; Ortmann, F.; Leo, K. Molecular parameters responsible for thermally activated transport in doped organic semiconductors. *Nat. Mater.* **2019**, *18*, 242−248.

(8) Kitaigorodsky, A. I. *Mixed Crystals*; Springer Berlin Heidelberg, 1984.

(9) Goetz, K. P.; Tsutsumi, J.; Pookpanratana, S.; Chen, J.; Corbin, N. S.; Behera, R. K.; Coropceanu, V.; Richter, C. A.; Hacker, C. A.; Hasegawa, T.; Jurchescu, O. D. Polymorphism in the 1:1 Charge-Transfer Complex DBTTF−TCNQ and Its Effects on Optical and Electronic Properties. *Adv. Electron. Mater.* **2016**, *2*, 1600203.

(10) Beyer, P.; Pham, D.; Peter, C.; Koch, N.; Meister, E.; Brütting, W.; Grubert, L.; Hecht, S.; Nabok, D.; Cocchi, C.; Draxl, C.; Opitz, A. State-of-Matter-Dependent Charge-Transfer Interactions between Planar Molecules for Doping Applications. *Chem. Mater.* **2019**, *31*, 1237−1249.

(11) Méndez, H.; Heimel, G.; Winkler, S.; Frisch, J.; Opitz, A.; Sauer, K.; Wegner, B.; Oehzelt, M.; Röthel, C.; Duhm, S.; Többens, D.; Koch, N.; Salzmann, I. Charge-transfer crystallites as molecular electrical dopants. *Nat. Commun.* **2015**, *6*, 8560.

(12) Opitz, A.; Duva, G.; Gebhardt, M.; Kim, H.; Meister, E.; Meisel, T.; Beyer, P.; Belova, V.; Kasper, C.; Pflaum, J.; Pithan, L.; Hinderhofer, A.; Schreiber, F.; Brütting, W. Thin films of electron donor−acceptor complexes: characterisation of mixed-crystalline phases and implications for electrical doping. *Mater. Adv.* **2022**, *3*, 1017−1034.

(13) Banerjee, R.; Hinderhofer, A.; Weinmann, M.; Reisz, B.; Lorch, C.; Gerlach, A.; Oettel, M.; Schreiber, F. Interrupted Growth to Manipulate Phase Separation in DIP:C60 Organic Semiconductor Blends. *J. Phys. Chem. C* **2018**, *122*, 1839−1845.

(14) Dieterle, J.; Broch, K.; Frank, H.; Duva, G.; Storzer, T.; Hinderhofer, A.; Novák, J.; Gerlach, A.; Schreiber, F. Delayed phase separation in growth of organic semiconductor blends with limited intermixing. *Phys. Status Solidi RRL* **2017**, *11*, 1600428.

(15) Tietze, M. L.; Benduhn, J.; Pahner, P.; Nell, B.; Schwarze, M.; Kleemann, H.; Krammer, M.; Zojer, K.; Vandewal, K.; Leo, K. Elementary steps in electrical doping of organic semiconductors. *Nat. Commun.* **2018**, *9*, 1182.

(16) Naab, B. D.; Zhang, S.; Vandewal, K.; Salleo, A.; Barlow, S.; Marder, S. R.; Bao, Z. Effective Solution- and Vacuum-Processed n-Doping by Dimers of Benzimidazoline Radicals. *Adv. Mater.* **2014**, *26*, 4268−4272.

(17) Tietze, M. L.; Pahner, P.; Schmidt, K.; Leo, K.; Lüssem, B. Doped Organic Semiconductors: Trap-Filling, Impurity Saturation, and Reserve Regimes. *Adv. Funct. Mater.* **2015**, *25*, 2701−2707.

(18) Olthof, S.; Mehraeen, S.; Mohapatra, S. K.; Barlow, S.; Coropceanu, V.; Brédas, J.-L.; Marder, S. R.; Kahn, A. Ultralow Doping in Organic Semiconductors: Evidence of Trap Filling. *Phys. Rev. Lett.* **2012**, *109*, 176601.

(19) Arkhipov, V. I.; Heremans, P.; Emelianova, E. V.; Bässler, H. Effect of doping on the density-of-states distribution and carrier hopping in disordered organic semiconductors. *Phys. Rev. B* **2005**, *71*, 045214.

(20) Arkhipov, V. I.; Emelianova, E. V.; Heremans, P.; Bässler, H. Analytic model of carrier mobility in doped disordered organic semiconductors. *Phys. Rev. B* **2005**, *72*, 235202.

(21) Mityashin, A.; Olivier, Y.; Van Regemorter, T.; Rolin, C.; Verlaak, S.; Martinelli, N. G.; Beljonne, D.; Cornil, J.; Genoe, J.; Heremans, P. Unraveling the Mechanism of Molecular Doping in Organic Semiconductors. *Adv. Mater.* **2012**, *24*, 1535−1539.

(22) Coropceanu, V.; Cornil, J.; da Silva Filho, D. A.; Olivier, Y.; Silbey, R.; Brédas, J.-L. Charge Transport in Organic Semiconductors. *Chem. Rev.* **2007**, *107*, 926−952.

(23) Menke, T.; Ray, D.; Meiss, J.; Leo, K.; Riede, M. In-situ conductivity and Seebeck measurements of highly efficient n-dopants in fullerene C_{60}. *Appl. Phys. Lett.* **2012**, *100*, 093304.

(24) Warren, R.; Blom, P. W. M.; Koch, N. Molecular p-doping induced dielectric constant increase of polythiophene films determined by impedance spectroscopy. *Appl. Phys. Lett.* **2023**, *122*, 152108.

(25) Yang, X.; Liu, J.; Koster, L. J. A. The Exceptionally High Dielectric Constant of Doped Organic Semiconductors. *Adv. Electron. Mater.* **2025**, *11*, 2400413.

(26) Kistenmacher, T. J.; Emge, T. J.; Wiygul, F. M.; Bryden, W. A.; Chappell, J. S.; Stokes, J. P.; Chiang, L. Y.; Cowan, D. O.; Bloch, A. N. DBTTF-TCNQ: A fractionally-charged organic salt with a mixed-stack crystalline motif. *Solid State Commun.* **1981**, *39*, 415−417.

(27) Emge, T. J.; Bryden, W. A.; Wiygul, F. M.; Cowan, D. O.; Kistenmacher, T. J.; Bloch, A. N. Structure of an organic charge-transfer salt derived from dibenzotetrathiafulvalene and tetrafluorotetracyanoquinodimethane (DBTTF−TCNQF4). Observation of a high-temperature phase transition. *J. Chem. Phys.* **1982**, *77*, 3188−3197.

(28) Mas-Torrent, M.; Hadley, P.; Bromley, S. T.; Crivillers, N.; Veciana, J.; Rovira, C. Single-crystal organic field-effect transistors based on dibenzo-tetrathiafulvalene. *Appl. Phys. Lett.* **2005**, *86*, 012110.

https://doi.org/10.1021/acs.chemmater.6c00277
Chem. Mater. 2026, 38, 4726−4737

(29) Yamada, T.; Hasegawa, T.; Hiraoka, M.; Matsui, H.; Tokura, Y.; Saito, G. Control of film morphology and its effects on subthreshold characteristics in dibenzotetrathiafulvalene organic thin-film transistors. *Appl. Phys. Lett.* **2008**, *92*, 233306.
(30) Gao, C.-H.; Zhu, X.-Z.; Zhang, L.; Zhou, D.-Y.; Wang, Z.-K.; Liao, L.-S. Comparative studies on the inorganic and organic p-type dopants in organic light-emitting diodes with enhanced hole injection. *Appl. Phys. Lett.* **2013**, *102*, 153301.
(31) Christodoulou, C.; Giannakopoulos, A.; Nardi, M. V.; Ligorio, G.; Oehzelt, M.; Chen, L.; Pasquali, L.; Timpel, M.; Giglia, A.; Nannarone, S.; Norman, P.; Linares, M.; Parvez, K.; Müllen, K.; Beljonne, D.; Koch, N. Tuning the Work Function of Graphene-on-Quartz with a High Weight Molecular Acceptor. *J. Phys. Chem. C* **2014**, *118*, 4784−4790.
(32) Konarev, D. V.; Khasanov, S. S.; Kuzmin, A. V.; Mikhailenko, M. V.; Otsuka, A.; Yamochi, H.; Kitagawa, H.; Lyubovskaya, R. N. Solid-State Properties of Hexaazatriphenylenehexacarbonitrile HAT-$(CN)^-_6$ Radical Anions in Crystalline Salts Containing Cryptand(M^+) and Crystal Violet Cations. *Chem. Eur. J.* **2020**, *26*, 17470−17480.
(33) Liang, Y.; Xing, W.; Liu, L.; Sun, Y.; Xu, W.; Zhu, D. Charge transport behaviors of a novel 2:1 charge transfer complex based on coronene and $HAT(CN)_6$. *Org. Electron.* **2020**, *78*, 105608.
(34) Opitz, A.; Peter, C.; Wegner, B.; Matte, H. R.; Röttger, A.; Florian, T.; Xu, X.; Beyer, P.; Grubert, L.; Hecht, S.; Belova, V.; Hinderhofer, A.; Schreiber, F.; Kasper, C.; Pflaum, J.; Zhang, Y.; Barlow, S.; Marder, S. R.; Koch, N. Ordered Donor−Acceptor Complex Formation and Electron Transfer in Co-deposited Films of Structurally Dissimilar Molecules. *J. Phys. Chem. C* **2020**, *124*, 11023−11031.
(35) Ahsan, M. R.; Singh, L.; Sar, B.; Mukherjee, A. Structural Variability in Cocrystals: Occurrence of Variable Stoichiometry and High Z' Forms in a Cocrystal System. *Cryst. Growth Des.* **2024**, *24*, 1695−1704.
(36) Lapkin, D.; Nasro, R.; Hagara, J.; Hofferberth, B.; Hinderhofer, A.; Gerlach, A.; Schreiber, F. Vacuum chamber for deposition of gradient thin films: Toward high-throughput structure−property correlative studies. *Rev. Sci. Instrum.* **2025**, *96*, 053905.
(37) Yadav, A.; Panda, D. K.; Zhang, S.; Zhou, W.; Saha, S. Electrically Conductive 3D Metal-Organic Framework Featuring π-Acidic Hexaazatriphenylene Hexacarbonitrile Ligands with Anion-π Interaction and Efficient Charge-Transport Capabilities. *ACS Appl. Mater. Interfaces* **2020**, *12*, 40613−40619.
(38) Valencia, A. M.; Schraut-May, L.; Siegert, M.; Hammer, S.; Cula, B.; Friedrich, A.; Helten, H.; Pflaum, J.; Cocchi, C.; Opitz, A. Unveiling the Role of Solvents in DBTTF:HATCN Ternary Cocrystals. *Chem. Mater.* **2026**, *38*, 2215−2226.
(39) Als-Nielsen, J.; McMorrow, D. *Elements of Modern X-ray Physics*; Wiley, 2011.
(40) Hinderhofer, A.; Hagenlocher, J.; Gerlach, A.; Krug, J.; Oettel, M.; Schreiber, F. Nonequilibrium Roughness Evolution of Small Molecule Mixed Films Reflecting Equilibrium Phase Behavior. *J. Phys. Chem. C* **2022**, *126*, 11348−11357.
(41) Saragi, T. P.; Reichert, T.; Scheffler, A.; Kussler, M.; Salbeck, J. Electron mobility in hexaazatriphenylene hexacarbonitrile field-effect transistors. *Synth. Met.* **2012**, *162*, 1572−1576.
(42) Casado, J.; Zgierski, M. Z.; Delgado, M. C. R.; Navarrete, J. T. L.; Mas-Torrent, M.; Rovira, C. Tetrathiafulvalene-based materials for organic field effect transistors. Inspection of their semiconductor properties by means of molecular spectroscopy and quantum chemistry. *J. Phys. Chem. C* **2007**, *111*, 10110−10118.
(43) Johnson, P. S.; Boukahil, I.; Himpsel, F. J.; Kearns, K. L.; Kang, J. H.; Lin, J.-C.; Leugers, A.; Meyers, G.; Mukhopadhyay, S.; Jackson, D. H. K.; Kuech, T. F. Multitechnique Approach for Determining Energy Levels and Exciton Binding Energies of Molecules for Organic Electronics. *J. Phys. Chem. C* **2016**, *120*, 1366−1374.
(44) Broch, K.; Dieterle, J.; Branchi, F.; Hestand, N. J.; Olivier, Y.; Tamura, H.; Cruz, C.; Nichols, V. M.; Hinderhofer, A.; Beljonne, D.; Spano, F. C.; Cerullo, G.; Bardeen, C. J.; Schreiber, F. Robust singlet fission in pentacene thin films with tuned charge transfer interactions. *Nat. Commun.* **2018**, *9*, 954.
(45) Schlaf, R.; Murata, H.; Kafafi, Z. Work function measurements on indium tin oxide films. *J. Electron Spectrosc. Relat. Phenom.* **2001**, *120*, 149−154.
(46) Bagus, P. S.; Staemmler, V.; Wöll, C. Exchangelike Effects for Closed-Shell Adsorbates: Interface Dipole and Work Function. *Phys. Rev. Lett.* **2002**, *89*, 096104.
(47) Koch, N.; Kahn, A.; Ghijsen, J.; Pireaux, J.-J.; Schwartz, J.; Johnson, R. L.; Elschner, A. Conjugated organic molecules on metal versus polymer electrodes: Demonstration of a key energy level alignment mechanism. *Appl. Phys. Lett.* **2003**, *82*, 70−72.
(48) Oehzelt, M.; Koch, N.; Heimel, G. Organic semiconductor density of states controls the energy level alignment at electrode interfaces. *Nat. Commun.* **2014**, *5*, 4174.
(49) Zhai, T.; Wang, R.; Katase, T.; Quigley, F.; Ohta, H.; Amsalem, P.; Koch, N.; Duhm, S. Substrate-Independent Energy-Level Pinning of an Organic Semiconductor Providing Versatile Hole-Injection Electrodes. *ACS Appl. Electron. Mater.* **2020**, *2*, 3994−4001.
(50) Lee, S.; Lee, J. H.; Kim, K. H.; Yoo, S. J.; Kim, T. G.; Kim, J. W.; Kim, J. J. Determination of the interface energy level alignment of a doped organic hetero-junction using capacitance-voltage measurements. *Org. Electron.* **2012**, *13*, 2346−2351.
(51) Sato, N.; Inokuchi, H.; Shirotani, I. Polarization energies of tetrathiafulvalene derivatives. *Chem. Phys.* **1981**, *60*, 327−333.
(52) Nielsen, P. Substrate dependent ionization and polarization energies of molecules: Dibenztetrathiafulvalene. *Solid State Commun.* **1978**, *26*, 835−838.
(53) Krause, S. Determination of the transport levels in thin films of organic semiconductors. Doctoral Thesis, Universität Würzburg, 2009.
(54) Hill, I.; Kahn, A.; Soos, Z.; Pascal, R. A., Jr Charge-separation energy in films of π-conjugated organic molecules. *Chem. Phys. Lett.* **2000**, *327*, 181−188.
(55) Chappell, J. S.; Bloch, A. N.; Bryden, W. A.; Maxfield, M.; Poehler, T. O.; Cowan, D. O. Degree of charge transfer in organic conductors by infrared absorption spectroscopy. *J. Am. Chem. Soc.* **1981**, *103*, 2442−2443.
(56) Grobman, W. D.; Pollak, R. A.; Eastman, D. E.; Maas, E. T.; Scott, B. A. Valence Electronic Structure and Charge Transfer in Tetrathiofulvalinium Tetracyanoquinodimethane (TTF-TCNQ) from Photoemission Spectroscopy. *Phys. Rev. Lett.* **1974**, *32*, 534−537.
(57) Grobman, W. D.; Silverman, B. D. Intramolecular screening of crystal fields and the X-ray-photoemission determination of charge transfer in TTF-TCNQ. *Solid State Commun.* **1976**, *19*, 319−322.
(58) Goetz, K. P.; Tsutsumi, J.; Pookpanratana, S.; Chen, J.; Corbin, N. S.; Behera, R. K.; Coropceanu, V.; Richter, C. A.; Hacker, C. A.; Hasegawa, T.; Jurchescu, O. D. Reply to Comment on Polymorphism in the 1:1 Charge-Transfer Complex DBTTF-TCNQ and Its Effects on Optical and Electronic Properties. *Adv. Energy Mater.* **2017**, *3*, 1600521.
(59) Rußegger, N.; Valencia, A. M.; Merten, L.; Zwadlo, M.; Duva, G.; Pithan, L.; Gerlach, A.; Hinderhofer, A.; Cocchi, C.; Schreiber, F. Molecular Charge Transfer Effects on Perylene Diimide Acceptor and Dinaphthothienothiophene Donor Systems. *J. Phys. Chem. C* **2022**, *126*, 4188−4198.
(60) Mallela, N. R.; Kawamoto, T.; Mori, T. Charge Polarity Control in Organic Transistors of Mixed and Segregated Complexes Based on Diaminonaphthalene and Pyrene. *ACS Appl. Mater. Interfaces* **2023**, *15*, 45201−45211.
(61) Abukaev, A.; Völter, C.; Romodin, M.; Schwartzkopff, S.; Bertram, F.; Konovalov, O.; Hinderhofer, A.; Lapkin, D.; Schreiber, F. pygid: a Python Package for Fast Data Reduction in Grazing-Incidence Diffraction (GID). *J. Appl. Crystallogr.* **2026**, *59*, 263−275.
(62) Nečas, D.; Klapetek, P. Gwyddion: an open-source software for SPM data analysis. *Cent. Eur. J. Phys.* **2012**, *10*, 181−188.

https://doi.org/10.1021/acs.chemmater.6c00277
Chem. Mater. 2026, 38, 4726−4737